University of California
Los Angeles

Mid-rapidity Λ and $\bar{\Lambda}$ Production in Au+Au Collisions at the Relativistic Heavy Ion Collider

A dissertation submitted in partial satisfaction
of the requirements for the degree
Doctor of Philosophy in Physics

by

Hui Long

2002

The dissertation of Hui Long is approved.

Chentao Lin

David Saltzberg

Charles A. Whitten Jr., Committee Co-chair

Huan Z. Huang, Committee Co-chair

University of California, Los Angeles

2002

To my very supportive family...

Table of Contents

1 Introduction **1**

2 Physics **4**

2.1 The Hadron Bag Model and the Critical Temperature 4

2.2 Nucleus-Nucleus Collisions 5

2.3 Λ ($\bar{\Lambda}$) and Strangeness Production 8

3 Facilities **17**

3.1 RHIC Accelerator Complex 17

3.2 The STAR Detector 19

4 Simulation and TPC Response Simulator **31**

4.1 GEANT4 and GSTAR 31

4.2 TPC Response Simulator 33

4.2.1 Charge Re-distribution 33

4.2.2 Drift of Electrons in the TPC 37

4.2.3 Amplification of Ionization 42

4.2.4 Signal Generation 46

4.2.5 Digitization 56

4.3 Evaluation of the TRS 56

5 Analysis Methods **76**

5.1 Trigger 76

5.2 Event Selection 76
5.3 Λ and $\bar{\Lambda}$ Reconstruction 78
5.4 Λ and $\bar{\Lambda}$ Signals and Backgrounds 83
5.5 Efficiency Corrections 98

6 Results 106
6.1 Corrected p_t Spectra 106
6.2 The Transverse Mass Distribution 106
6.3 Ratio of the $\bar{\Lambda}/\Lambda$ 109
6.4 The dN/dy and h^- 111

7 Systematic Uncertainties 116
7.1 Uncertainties in the Efficiency Calculation 116
7.2 Uncertainties in Raw Signal Extraction 118
7.3 Sector-by-Sector Variations and other Asymmetries 122
7.4 Other Uncertainties 126
7.5 Feed-Down Contributions 127
7.6 Double-Counting Signals 132

8 Discussion 141
8.1 Lambda/Anti-Lambda Production 141
8.2 Lambda Enhancement from pp to AA Collisions 146
8.3 Simple Thermal Model and Baryon Yield 147
8.4 Conclusions 150

A Relativistic Kinematics 152

A.1 Lorentz Transformations 152

A.2 Kinematic Variables 153

B The STAR Collaboration 155

C Data Tables 159

References 170

List of Figures

1.1 QCD phase diagram 3

2.1 Space-time Picture of a Nucleus-Nucleus Collision 6

2.2 K/π Ratio and ϕ/π Ratio 9

2.3 Strange Particle Enhancement versus Strangeness Content (WA97) 10

2.4 Mid-Rapidity $m_\perp$-Spectra of Λ, Ξ^- and Ω^- and Antihyperons . . 11

2.5 M_T Slope and mass 12

2.6 $\bar{B}/B$ ratio vs. $\sqrt{s_{NN}}$ 13

2.7 Ratio of $\bar{\Lambda}/\bar{p}$ from NA35 15

2.8 Ratio of $\bar{\Lambda}/\bar{p}$ (AGS) 16

3.1 Diagram of the AGS - RHIC facility 18

3.2 First collision at $\sqrt{s_{NN}} = 60$ GeV 20

3.3 First collision at $\sqrt{s_{NN}} = 130$ GeV 21

3.4 The STAR experiment 22

3.5 The STAR Magnetic Field Map 23

3.6 The 3D view of ExB distortion 24

3.7 The STAR Time Projection Chamber 24

3.8 The Wires and Pads Layout 26

3.9 A TPC Super-Sector 27

3.10 Resistors for the Outer Field Cage 28

4.1 The Drift Field Lines in a typical MWPC 34

4.2 The Charge Segment 35
4.3 Transverse Diffusion Constant vs. B^2 38
4.4 Side View of the Drifting Electron 39
4.5 **E** Field Lines in the MWPC (inner sector) 40
4.6 **E** Field Lines in MWPC (outer sector) 41
4.7 Schematic Development of The Avalanche on the Anode Wires . . 43
4.8 Change in Gain vs. Change in Pressure in the STAR TPC 45
4.9 Plot of S(t) on a logarithmic time scale 47
4.10 Calculation of Signal Currents Induced on Pad Plane 49
4.11 Charge Images Created by a Charge q 50
4.12 Charge Collected by Pad 51
4.13 3D View of the Pad Response Function (PRF) 59
4.14 Projected View of the PRF on the X axis (outer) 60
4.15 Projected View of the PRF on the X axis (inner) 61
4.16 The Measured PRF on the X axis (inner) 62
4.17 Projected View of the PRF on the Y axis (outer) 63
4.18 Projected View of the PRF on the Y axis (inner) 64
4.19 Projected View of the PRF on the X axis (outer, all wire) 65
4.20 Pre-amplifier and shaper 66
4.21 Number of Pads per Hit (TRS) 67
4.22 Number of Pads per Hit (Real) 68
4.23 Number of Time-Buckets per Hit (TRS) 69
4.24 Number of Time-Buckets per Hit (Real) 70

4.25 XY Residuals vs. Crossing Angle (Outer Sector) 71
4.26 Z Residuals vs. dip Angle (Outer Sector) 72
4.27 XY Residual Dependence on Drift Length (Real Data) 73
4.28 XY Residual Dependence on Drift Length (TRS Data) 74
4.29 Mean Energy Deposited per Hit vs. Pad Row 75
4.30 Distribution of the Number of Hits per Track 75

5.1 Minimum-bias charged multiplicity distribution 77
5.2 Lambda Decay Topology 79
5.3 The measured $\langle dE/dx \rangle$ vs. p for reconstructed tracks in the TPC 81
5.4 The Crossing points of two circles 82
5.5 Invariant mass distribution of Λ and $\overline{\Lambda}$ candidates. 84
5.6 Comparison Between Lorentzian Fit and Gaussian Fit 85
5.7 Mass Histograms of Signals and Combinatorial Background 86
5.8 Raw yield ($0.4 < P_t < 0.6$ GeV/c) 88
5.9 Raw yield ($0.6 < P_t < 0.8$ GeV/c) 89
5.10 Raw yield ($0.8 < P_t < 1.0$ GeV/c) 90
5.11 Raw yield ($1.0 < P_t < 1.2$ GeV/c) 91
5.12 Raw yield ($1.2 < P_t < 1.4$ GeV/c) 92
5.13 Raw yield ($1.4 < P_t < 1.6$ GeV/c) 93
5.14 Raw yield ($1.6 < P_t < 1.8$ GeV/c) 94
5.15 Raw yield ($1.8 < P_t < 2.0$ GeV/c) 95
5.16 Raw yield ($2.0 < P_t < 2.2$ GeV/c) 96

5.17 Raw yield ($2.2 < P_t < 2.4$ GeV/c) 97
5.18 Event Embedding Procedure 98
5.19 Number of common hits vs. number of fit points 99
5.20 Reconstruction efficiency of the Λ for 5 centrality bins 101
5.21 Reconstruction efficiency of the $\bar{\Lambda}$ for 5 centrality bins 102
5.22 Reconstruction Efficiency of the Λ in $p_t - Rapidity$ Phase Space . 103
5.23 Uncorrected Transverse Momentum Spectra of the Λ for 5 centrality bins 104
5.24 Uncorrected Transverse Momentum Spectra of the $\bar{\Lambda}$ for 5 centrality bins 105

6.1 Corrected Transverse Momentum Spectra of the Λ for 5 centrality bins 107
6.2 Corrected Transverse Momentum Spectra of the $\bar{\Lambda}$ for 5 centrality bins 108
6.3 Transverse Mass Spectra for 5 Centrality Bins for Λ 112
6.4 Transverse Mass Spectra for 5 Centrality Bins for $\bar{\Lambda}$ 113
6.5 Ratio of the $\bar{\Lambda}/\Lambda$ for 5 centrality bins 114
6.6 dndy vs. h^- 115

7.1 Cuts comparison (1) 119
7.2 Cuts comparison (2) 122
7.3 Cuts comparison (3) 123
7.4 Cuts comparison (4) 124
7.5 Cuts comparison (5) 125

7.6 Cuts comparison (6) 126
7.7 Cuts comparison (7) 127
7.8 Cuts comparison (8) 128
7.9 Cuts comparison (9) 129
7.10 Cuts comparison (10) 130
7.11 Cuts comparison (11) 131
7.12 Cuts comparison (12) 132
7.13 Number of Reconstructed Λ vs. Sector 136
7.14 Number of Reconstructed Λ vs. Sector ($1.0 < p_t < 1.2$ GeV/c) . . 137
7.15 Relative Efficiency vs. p_t 138
7.16 The dcaV0 Distribution from Real Data and MC Data 139
7.17 The m_t Spectra of the Λ from Feedown 140

8.1 The mid-rapidity $\overline{\Lambda}$ ($|y|<0.5$) transverse momentum distribution from the top 5% most central collisions. For comparison the distributions for negative hadrons ($d^2N/(2\pi p_T)dp_T d\eta$, $|\eta|<0.1$) and anti-protons ($|y|<0.1$) for the similar centrality bin are included. Statistical errors of the data points are smaller than the marker size. 143
8.2 The mid-rapidity transverse momentum for $\overline{\Lambda}$ ($|y|<0.5$), negative hadrons ($d^2N/(2\pi p_T)dp_T d\eta$, $|\eta|<0.1$) and anti-protons ($|y|<0.1$) for central collisions. Statistical errors of the data points are smaller than the marker size. 144

8.3 Λ and $\overline{\Lambda}$ rapidity density as a function of negative hadron multiplicity at mid-rapidity. The open symbols in the figure are data points from an independent analysis using event-mixing techniques. Errors shown are statistical only. 145

8.4 Contribution for the Wroblewski factor from strange baryon (dotted line), strange mesons (dashed line) and mesons with hidden strangeness (dash-dotted line). The sum of all contributions is given by the full line. 146

8.5 The Λ/π^+ ratio vs $\sqrt{s}$. 148

8.6 The Λ/π^+ ratio vs $\sqrt{s}$. The ratio from AA collisions are normalized by a factor of 4.65 149

8.7 particle ratios from simple thermal model 150

8.8 N_p Vs. T 151

List of Tables

2.1 Properties of the Λ Baryon 8

3.1 Physical parameters and performance specifications for RHIC . . 18

3.2 Quantities measurable on an Event-By-Event basis 30

5.1 Centrality definitions 78

5.2 Requirements placed on candidate positive and negative tracks . . 80

6.1 Data-points for Λ spectra 109

6.2 Data-points for $\bar{\Lambda}$ spectra 110

6.3 Fit parameters from exponential and Boltzmann fits of the m_T spect ra for Λ and $\overline{\Lambda}$. Both statistical (the first) and systematic errors are presented. 110

6.4 The corresponding h^- for 5 centrality bins 111

7.1 Value of Signals Extracted by Different Methods 120

7.2 Relative Uncertainties in Different z Bins and Overall Uncertainties 121

7.3 Corrected Λ and Ratio of Efficiencies 133

7.4 Corrected Λ and Ratio of Efficiencies (II) 134

7.5 Corrected Number of Λ from Feed-down 135

7.6 Percentage of Double-Counted Signals 136

C.1 Λ Yield 0-5% Centrality Bin 160

C.2 Λ Yield 5-10% Centrality Bin 161

C.3 Λ Yield 10-20% Centrality Bin 162
C.4 Λ Yield 20-35% Centrality Bin 163
C.5 Λ Yield 35-75% Centrality Bin 164
C.6 $\bar{\Lambda}$ Yield 0-5% Centrality Bin 165
C.7 $\bar{\Lambda}$ Yield 5-10% Centrality Bin 166
C.8 $\bar{\Lambda}$ Yield 10-20% Centrality Bin 167
C.9 $\bar{\Lambda}$ Yield 20-35% Centrality Bin 168
C.10 $\bar{\Lambda}$ Yield 35-75% Centrality Bin 169

Acknowledgments

I thank H. Huang and C. Whitten for being the best advisors possible. Thanks also go to members of the UCLA Heavy Ion and Intermediate Energy group: G. Igo, S. Trentalange, V. Ghazikhanian, J. Kiryluk, O. Tsai, A. Tai, Y. Chen, P. Soresen, J. Wood and former graduate student E. Yamamoto and S. Kelly. Special thanks to Stephen Trentalange for useful advise on my data analysis and help with writing my thesis. I 'd also like to thank my ex-classmate Zhangbu Xu for his help with my analysis. Thanks to H. Caines, P. Jones, M.A.C. Lamont, G. Van Buren, H. Zhang and other members of the STAR strangeness group for their help with my analysis work. Thanks to H.G. Ritter, H. Wieman, J. Thomas, I. Sakrejda, R. Bossingham, N. Xu, E. Hjort, F. Wang, J. Porter, R. Snellings, D. Hardtke, B. Lasiuk, L. Ray, Y. Fisyaki, B. Stringfellow and P. Neviski for their help with my early work on the TPC alignment and simulations. Thanks to the whole STAR collaboration and the RHIC Operations Group.

Vita

16 Dec. 1971	Born, YueYang, Hunan, P.R.China
1994	B.S. Physics University of Science and Technology of China Anhui ,P.R.China
1997	Teaching Assistant Department of Physics University of California - Los Angeles
1997	M.S. Physics University of California - Los Angeles Los Angeles, CA
1997 – 2002	Graduate Research Assistant Heavy Ion and Intermediate Energy Physics Group University of California - Los Angeles

Publications and Presentations

K.H. Ackermann *et al.*, Hardware Controls for the STAR Experiment at RHIC, *IEEE Trans. Nucl. Sci.* **47**:210, 2000.

K.H. Ackermann *et al.*, The STAR Time Projection Chamber, *Nucl. Phys.* **A661**:681, 2000.

K.H. Ackermann *et al.*, Elliptic Flow in Au+Au Collisions at $\sqrt{s_{NN}} = 130$ GeV, *Phys. Rev. Lett.*, **86**:402, 2001.

K.N. Barish *et al.*, Leading Baryon and Antiproton Measurements in P + A Collisions at AGS Energies, *Nucl. Phys.*, **A698**:599, 2002.

K.N. Barish *et al.*, Leading Baryon Production in P + A Collisions at Relativistic Energies, *Phys. Rev.*, **C65**:014904, 2002.

C. Adler *et al.*, Results from the STAR Experiment, *Nucl. Phys.*, **A698**:64, 2002.

C. Adler *et al.*, Measurement of inclusive antiprotons from Au+Au collisions at $\sqrt{s_{NN}} = 130$ GeV, *Phys. Rev. Lett.*, **87**:262302-1, 2001.

C. Adler *et al.*, Antideuteron and Antihelium Production in Au+Au collisions at $\sqrt{s_{NN}} = 130$ GeV, *Phys. Rev. Lett.*, **87**:262301-1, 2001.

C. Adler *et al.*, Identified Particle Elliptic Flow in Au+Au collisions at $\sqrt{s_{NN}} =$ 130 GeV, *Phys. Rev. Lett.*, **87**:182301-1, 2001.

C. Adler *et al.*, Multiplicity Distribution of Negatively Charged Hadrons in Au+Au Collisions at $\sqrt{s_{NN}} = 130$ GeV, Accepted by *Phys. Rev. Lett.* 16 July, 2001.

C. Adler *et al.*, Pion Interferometry of $\sqrt{s_{NN}} = 130$ GeV Au+Au Collisions at RHIC, Accepted by *Phys. Rev. Lett.* 11 July, 2001.

C. Adler *et al.*, Midrapidity $Antiproton-to-Proton$ Ratio in Au+Au Collisions at $\sqrt{s_{NN}} = 130$ GeV, Accepted by *Phys. Rev. Lett.* **86**:4778, 2001.

H. Long, Mid-rapidity Λ and $\bar{\Lambda}$ Production in Au+Au collisions at $\sqrt{s_{NN}} =$ 130 GeV, *Contribution to the American Physical Society Meeting*, 2001.

H. Long, First look at Strangeness at RHIC with the STAR detector, *Contribution to the American Physical Society Meeting*, 2000.

H. Long, Study of the v0 reconstruction with the STAR TPC, *Contribution to the American Physical Society Meeting,* 1998.

Abstract of the Dissertation

Mid-rapidity Λ and $\bar{\Lambda}$ Production in Au+Au Collisions at the Relativistic Heavy Ion Collider

by

Hui Long

Doctor of Philosophy in Physics

University of California, Los Angeles, 2002

Professor Huan Z. Huang, Co-chair

Professor Charles A. Whitten Jr., Co-chair

Results from the first measurement of mid-rapidity Λ ($\bar{\Lambda}$) production in Au+Au collisions at RHIC ($\sqrt{s_{NN}} = 130$ GeV) are described. Using the STAR detector, Λ ($\bar{\Lambda}$) baryons were measured from the $\Lambda \to \pi^- p$ and $\bar{\Lambda} \to \pi^+ \bar{p}$ decay channels. The transverse mass spectra of the Λ and $\bar{\Lambda}$ are found to be well discribed by a Boltzman function. The rapidity density and the slope parameter are obtained for several centrality bins. For the 5% most central collisions, the yield dN/dy is $17.0 \pm 0.4(stat) \pm 1.8(sys)$ and $12.0 \pm 0.3(stat) \pm 1.3(sys)$ for Λ and $\bar{\Lambda}$ respectively. The feed-down effects from multi-strangeness particle decay were estimated for the most central bin and it is about 27% of the inclusive measurement. The slope parameter varies from 312 MeV for the most central collisions to 254 MeV for the peripheral collisions. This trend is indicative of larger expansion velocities for the Λs and $\bar{\Lambda}$s in the central collision than in the peripheral collisions. The $\bar{\Lambda}$ to Λ ratio is 0.74 ± 0.04, consistant with a low net baryon density at mid-rapidity, and with no significant variation over the range of 5 selected centrality bins. The p_T distributions of Λ and $\bar{\Lambda}$ are considerably flatter than that of the

negative hadrons, indicating an increasingly important contribution from baryon production at high p_T. The rapidity densities of Λ and $\bar{\Lambda}$ are approximately proportional to the number of negative hadrons.

CHAPTER 1

Introduction

Relativistic heavy ion collisions provide a unique opportunity to study the properties of highly excited hadronic matter under extreme conditions of high density and high temperature [Red01]. It is generally believed that Quantum Chromodynamics (QCD) is the fundamental theory to describe and determine the Equation of State of such highly excited nuclear matter. In the QCD Theory, the strong force coupling constant depends on the distance scale of the interaction. When the distance is small, perturbative QCD is applicable and when it is large, one has to use lattice QCD. Lattice QCD indicates that when the distance scale becomes comparable to the size of hadron, quarks interact with an effective interaction which goes approximately linearly with the spatial distance [Won94]. This feature makes it more energetically favorable to produce another quark-antiquark pair than to break them up when trying to seperate a quark/anti-quark pair, or diquark. It therefore becomes an impossible task to isolate a quark from its partner, resulting in the confinement of quarks. On the other hand, if there is a finite system packed with enough quarks and gluons, the coupling between quarks will be small due to small coupling distances. This system will be different from the hadron system in the sense that quarks and gluons are not associated with individual hadrons and are considered quasi-free. This is commonly refered to as the Quark-Gluon Plasma. The phase transition from hadron matter to QGP can happen when the temperature is extremely high

or when the baryon density is large. This state of matter is believed to have existed in the early universe, about one microsecond after the Big Bang. Lattice QCD calculations also indicate that the order of the phase transition appears to depend on the quark masses [Got87].

Motivated by QCD predictions and calculations of this new form of matter, scientists around the world have studied heavy ion collisions in which the conditions to form the QGP can be met in the laboratory. Figure 1.1 shows the QCD phase diagram and possible accessible phases in nature and heavy ion collisions. Results from the Alternating Gradient Synchrotron (AGS) at Brookhaven and the CERN SPS have yielded some evidence which cannot be explained with existing models, for example a ρ mass shift, J/ψ suppression and strangeness enhancement. But whether they constitute the signatures for the formation of QGP is still not universally agreed upon.

Currently, scientists are studying heavy ion collisions using the Relativistic Heavy Ion Collider (RHIC) at Brookhaven National Laboratory. With center of mass collision energies 10 times greater than previous heavy ion studies and wider variability in the species of colliding particles, this machine offers greater opportunities in measuring the macroscopic properties of strongly interacting matter and the predicted phase transition back to normal matter. In turn, the experimental results will help better determine the dynamics of QCD interactions and the conditions prevalent in the early universe.

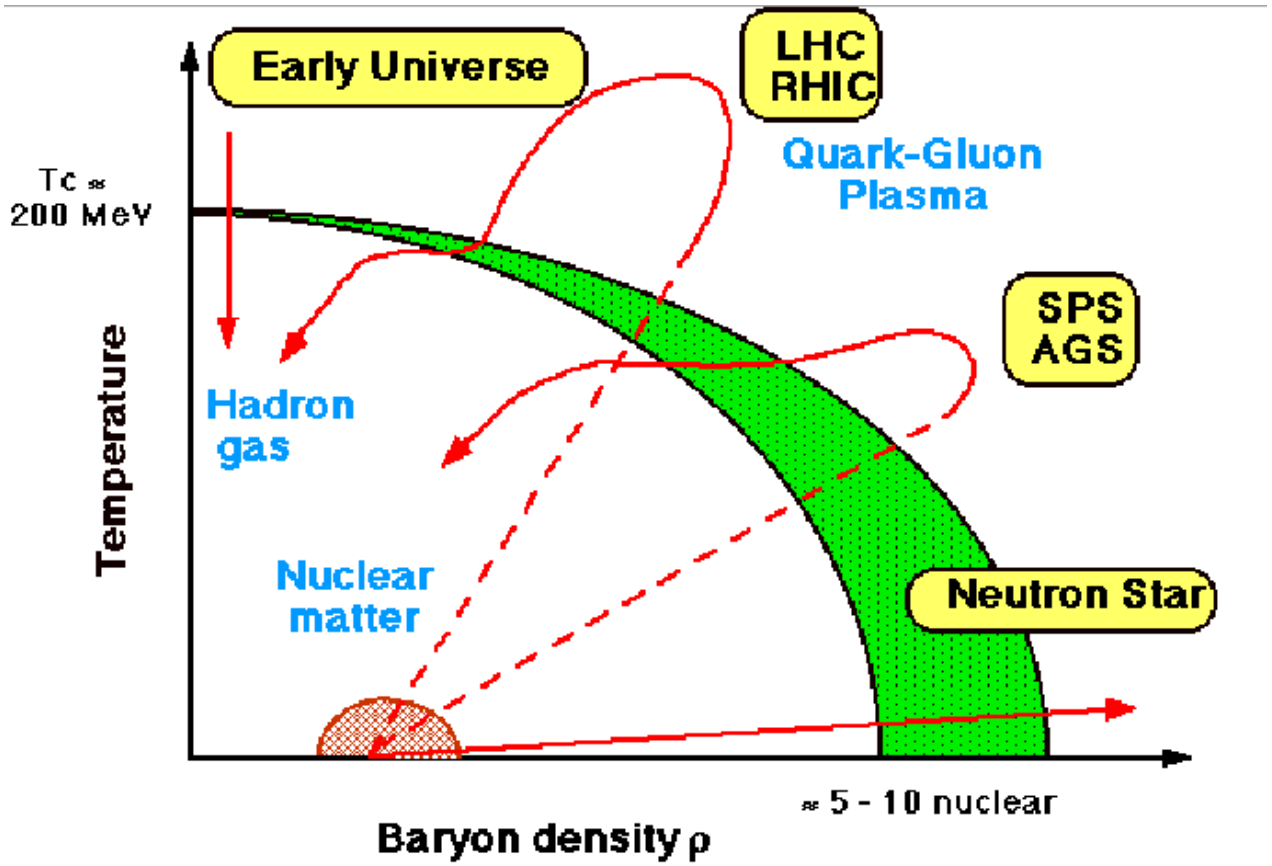

Figure 1.1: QCD phase diagram. The major features of QCD phases possibly accessible in nature and heavy ion collisions are shown. Figure taken from [Yam01].

CHAPTER 2

Physics

2.1 The Hadron Bag Model and the Critical Temperature

A phenomenological description of quark confinement is provided by the Bag Model[CJJ74][DD83]. In this model, quarks are treated as massless particles inside a bag of finite dimension and as infinitely massive outside the bag. Confinement in the model is the result of the balance of the bag pressure B, which is directed inward, and the tension arising from the kinetic energy of the quarks. If the quarks are confined in the bag, the gluons are as well.

We can get an estimate of the magnitude of the bag pressure by considering massless free fermions in a spherical cavity of radius R. The fermions in the cavity are described by the Dirac equation

$$\gamma \cdot p\psi = 0. \tag{2.1}$$

With the boundary condition $\bar{\psi}\psi = 0$ at the bag surface $r = R$ [Clo79], the energy of the quarks is

$$p^0 = \frac{2.04}{R}. \tag{2.2}$$

If we use the bag pressure B to represent confinement effects, the total energy for system of N quarks in a bag is

$$E = \frac{2.04N}{R} + \frac{4\pi}{3}R^3 B. \tag{2.3}$$

The equilibrium radius of the system is located at radius R determined by $dE/dR = 0$, which leads to

$$B^{1/4} = \left(\frac{2.04N}{4\pi}\right)^{1/4} \frac{1}{R}. \tag{2.4}$$

The bag pressure constant $B^{1/4}$ is 206 MeV for N=3 and R=0.8 fm.

For a QGP system in thermal equilibrium at high temperature T within volume, V, the pressure arising from the quarks, antiquarks and gluons can be calculated using classic quantum statistics techniques. The pressure is given by

$$P = g_{total}\frac{\pi^2}{90}T^4, \tag{2.5}$$

where

$$g_{total} = g_g + \frac{7}{8}(g_q + g_{\bar{a}}) = 37 \tag{2.6}$$

and g_g, g_q, g_q are degeneration numbers of (anti) quarks and gluons. The critical temerature is defined as the temperature when the QGP pressure is equal to the bag pressure. This is given by

$$T_c = (\frac{90}{37\pi^2})^{1/4}B^{1/4}. \tag{2.7}$$

Thus, we have $T_c = 144$ MeV for $B^{1/4} = 206$ MeV. When the temperature is higher than T_c, the bag will not be able to contain the quark matter and it will be deconfined to form the QGP. At the critical temperature of 144 MeV, the energy density of the QGP is about 0.68 GeV/fm^3.

2.2 Nucleus-Nucleus Collisions

The head-on collision of two nuclei can be represented as two thin disks approaching each other at high speed because of the Lorentz contraction effect in

the moving direction. The dynamics of the collision can be viewed from a different perspective in the space-time diagram with the longitudinal coordinate z and the time coordinate t, as shown in Fig. 2.1. The trajectories of the colliding projectile nucleus and target nucleus are shown as thick lines.

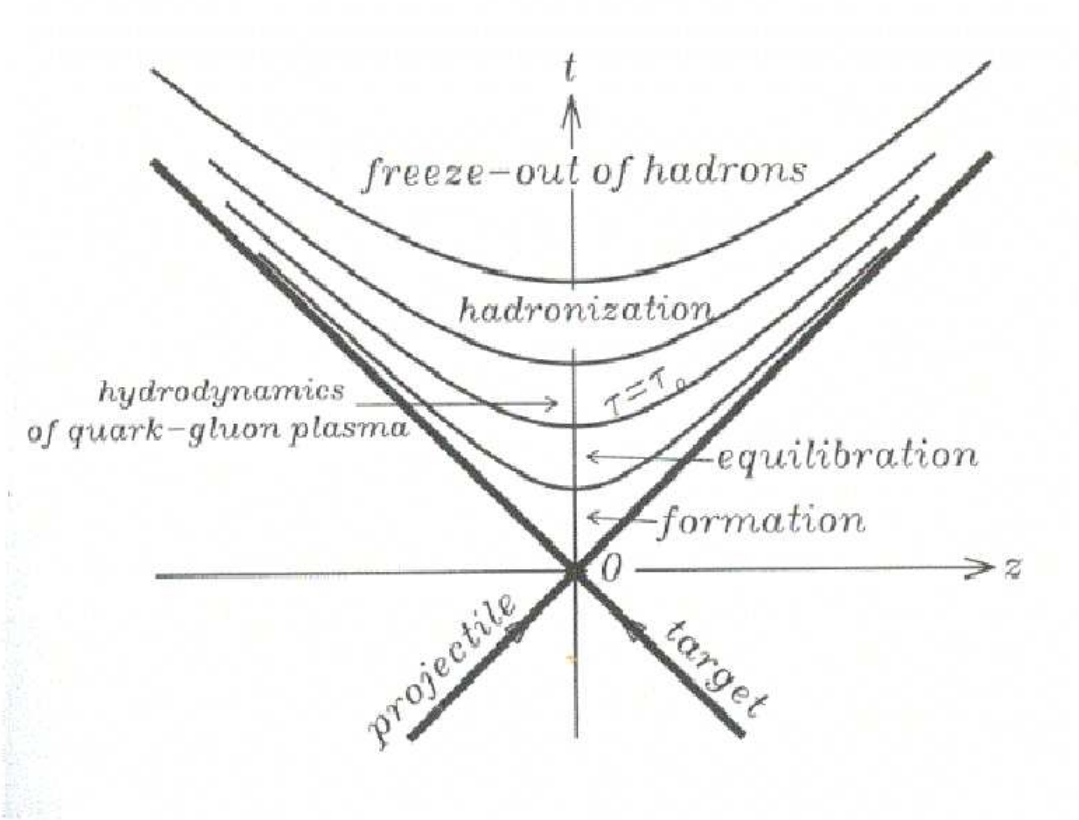

Figure 2.1: The Space-time picture of a nucleus-nucleus collision.

Each nucleus-nucleus collision consists of large number of nucleon-nucleon collisions and each inelastic nucleon-nucleon collision is accompanied by a large loss of energy of the colliding baryons. At very high energy (of the order of 100 GeV/nucleon and above in the center-of-mass system), the slowed-down baryons can still have enough momentum to proceed forward and move away from the collision region. So the collision region is a system with high energy density

and small net baryon density which is similar to conditions in the early universe. The physics in nucleus-nucleus collisions has lots of astrophysical interest[Bjo83].

High energy density means high system temperature. When the energy density is high enough, the system can be in the region of the QGP. Since all the deposited energy during a collision eventually manifests itself by producing particles which can be detected directly or indirectly , one can estimate the initial energy density [Bjo83] by

$$\epsilon = \frac{m_T}{\tau_0 A} \frac{dN}{dy}|_{y=0}. \tag{2.8}$$

This shows the energy density over the transverse area A at proper time τ_0 is proportional to the number of particles produced in the mid-rapidity region. m_T is the transverse mass of particles. This result was first derived by Bjorken [Bjo83]. The parameter τ_0 is the proper time at which the QGP is produced and it was estimated to be 1 fm/c [Bjo83]. For Au on Au collisions at RHIC at $\sqrt{s_{NN}} = 130$ GeV, $dNdy$ for negatively charged particles is about 280 and the $\langle P_T \rangle$ is 0.508 GeV/c [Adl01a]. If we assume all of them are pions, the estimated energy density is about 2.9 GeV/fm^3. This is greater than the energy density estimated for the QGP at the critical temperature.

From the space-time diagram, one can see the QGP takes a time to form and reach thermal equilibrium equal to the proper time, τ_0. After that, when the system continues to expand rapidly, the energy density drops and the transition from the QGP to hadron matter occurs at later times. The hadrons will stream out of the collision region when the temperature drops below the freeze-out temperature. What are directly observable are the particles after the freeze-out.

2.3 Λ ($\bar{\Lambda}$) and Strangeness Production

The Λ is a singlely strange hyperon with quark content (uds). $\bar{\Lambda}$ ($\bar{u}\bar{d}\bar{s}$) is its anti-particle. Its major properties are listed in Table 2.1.

Λ Baryon	
Mass	1115.684 MeV/c^2
τ (mean life)	2.632e-10 s
Major Branching Ratios	
$p\pi^-$	63.9%
$n\pi^0$	35.8%

Table 2.1: Properties of the Λ Baryon.

The production of strange (s) and anti-strange ($\bar{s}$) quarks was proposed by Rafelski [Raf82] as a probe to study the QGP phase transition. In a deconfined QGP, the $s\bar{s}$ pair can be copiously produced through gluon fusion ($gg \rightarrow s\bar{s}$)[Raf82, RR86]. The energy threshold for this strange quark production mechanism is roughly 2 times the mass of the s quarks which is about 150 MeV. This is much smaller than the threshold for strangeness production in the hadronic scenario. Therefore, it is considerably easier for a system to produce strange particles if it is in the QGP state than in the hadronic matter state. In pp or pA collisions, the created system is considered too small to hold a QGP. Therefore, these systems are usually used as the scaling reference to show the strangeness enhancement. At CERN SPS, the K/π ratio and the ϕ/π ratio have been seen as enhanced from pp or pA to S+S and Pb+Pb collisions [R01] (see Fig. 2.2). For strange hyperons, the enhancement increases with strangeness content [R01] as shown in Figure 2.3 where the enhancement, E, going from p+Pb to Pb+Pb collisions, is defined as the double ratio of the strange particle yield to

the number of participants, normalized to the ratio in p+Pb collisions. Although one can say that the QGP can lead to strangeness enhancement, the observation of the strangeness enhancement doesn't definitely imply the formation of QGP. There are conventional explanations for the enhancement at the CERN-SPS. The recent idea of antihyperon production by multi-mesonic reactions [Gre00] is just an example. In short, whether the enhancement signals the formation of a QGP is still an issue and more systematic studies are still needed at RHIC.

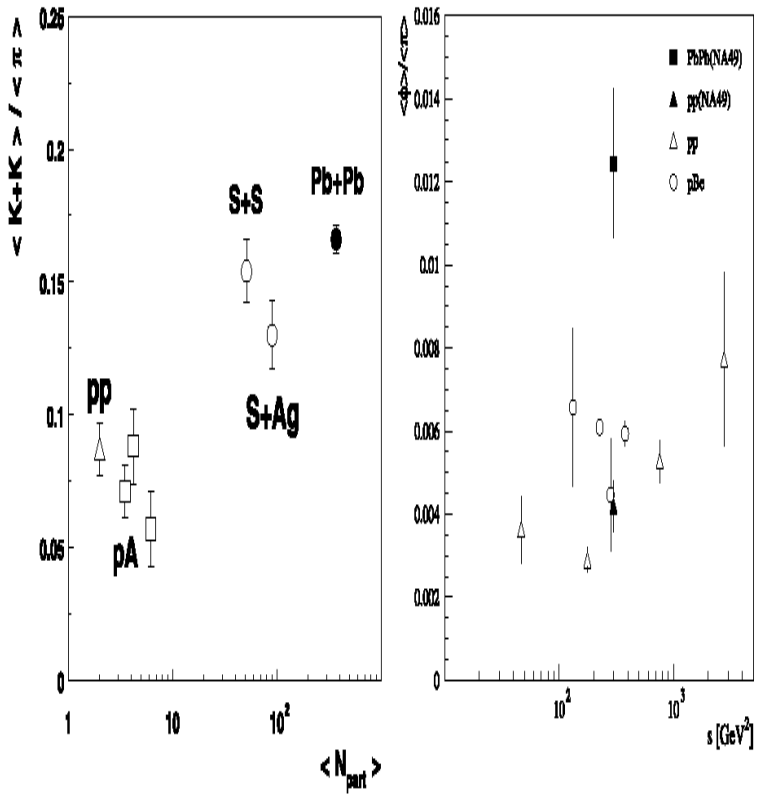

Figure 2.2: Left: Ratio of the multiplicity of kaons and pions for various target-projectile systems as function of the number of participants–global strangeness enhancement. Right: ϕ/π ratio measured for Pb+Pb (NA49) compared with p+p data (NA49). This figure taken from [R01].

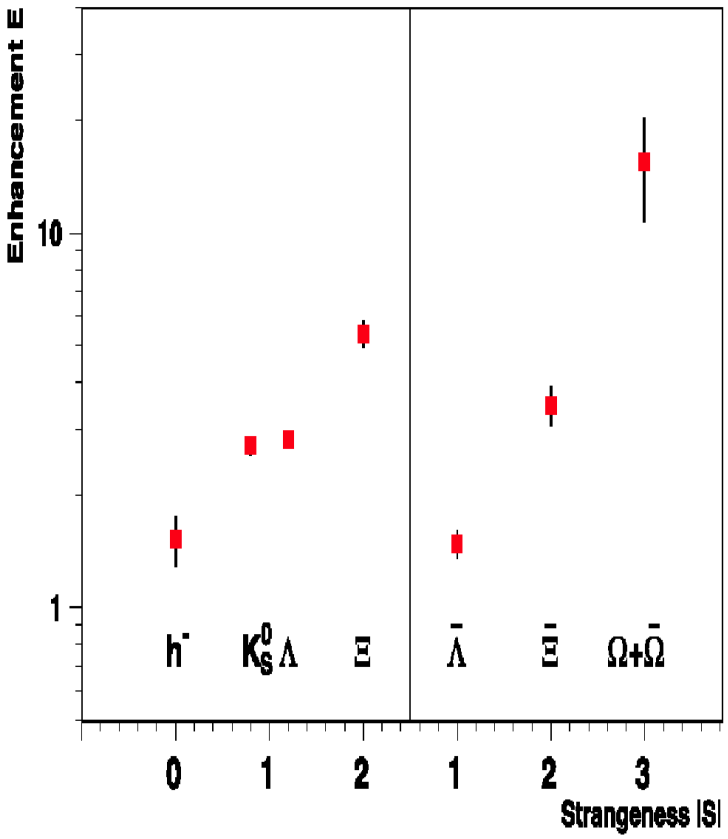

Figure 2.3: Strange particle enhancement versus strangeness content (WA97). This figure taken from [R01].

In addition to the issues related to the QGP, understanding the dynamic evolution of the system is also important. Figure 2.4 shows the mid-rapidity M_T spectra of Λ, Ξ^-, Ω^- and antihyperons in Pb+Pb collisions at CERN-SPS energy[Fin00]. We note the shape identity of the Λ and $\bar{\Lambda}$ spectra at a level of better than 1% (Figure 2.4. It has been argued that [Raf01a] the similarity in the hyperon and antihyperon spectra support a sudden hadronization picture: driven by internal pressure, a QGP fireball expands and ultimately a sudden breakup into final-state particles occurs, which reach detectors without much further rescattering. Deep supercooling requires a first order phase transition and

this in turn implies the presence of a latent heat[Raf01a]. It was also argued that because the Λ contains potentially two original valence quarks, the Λ-spectra are stretched in y, whereas $\bar{\Lambda}$ spectra are not, as they are from newly-formed particles. However, both have the same thermal-explosive collective-flow controlled shape of $m_\perp$-spectra.

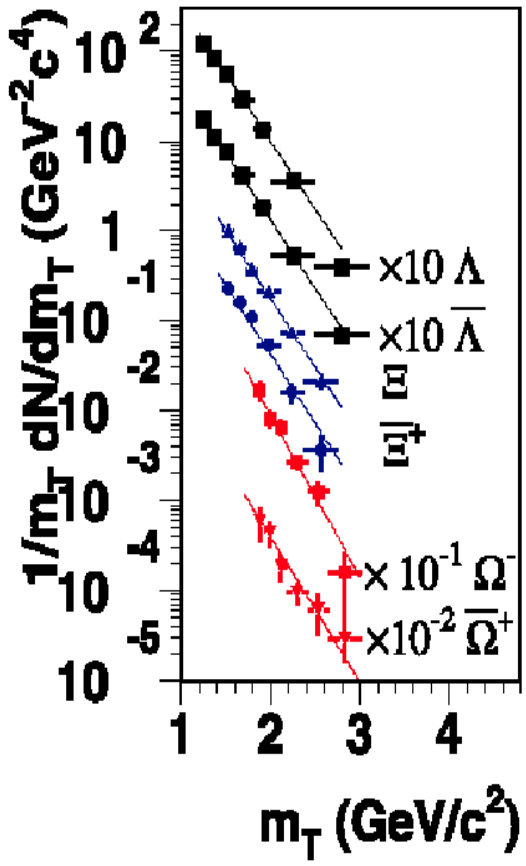

Figure 2.4: Mid-rapidity $m_\perp$-Spectra of Λ, Ξ^- and Ω^- and antihyperons obtained in 158 GeV/nucleon Pb-Pb interactions by the CERN WA97 experiment[Raf01a].

In a scenario where thermal motion is coupled with a transverse collective expansion, one can expect the measured slope parameter in m_t spectra to consist of two terms as

$$\langle T \rangle = T_0 + m\beta^2, \tag{2.9}$$

where T_0 is the thermal temperature and β is the common flow velocity. Figure 2.5 shows the dependence of the m_T spectra inverse slope, T, on the particle mass m for Pb+Pb collisions at SPS energy. It seems the multiple strangeness hyperons don't flow as much as the Λ. It would be very interesting to see if this flow picture is similar at the RHIC energy which is at almost 10 times higher collision center-of-mass energy.

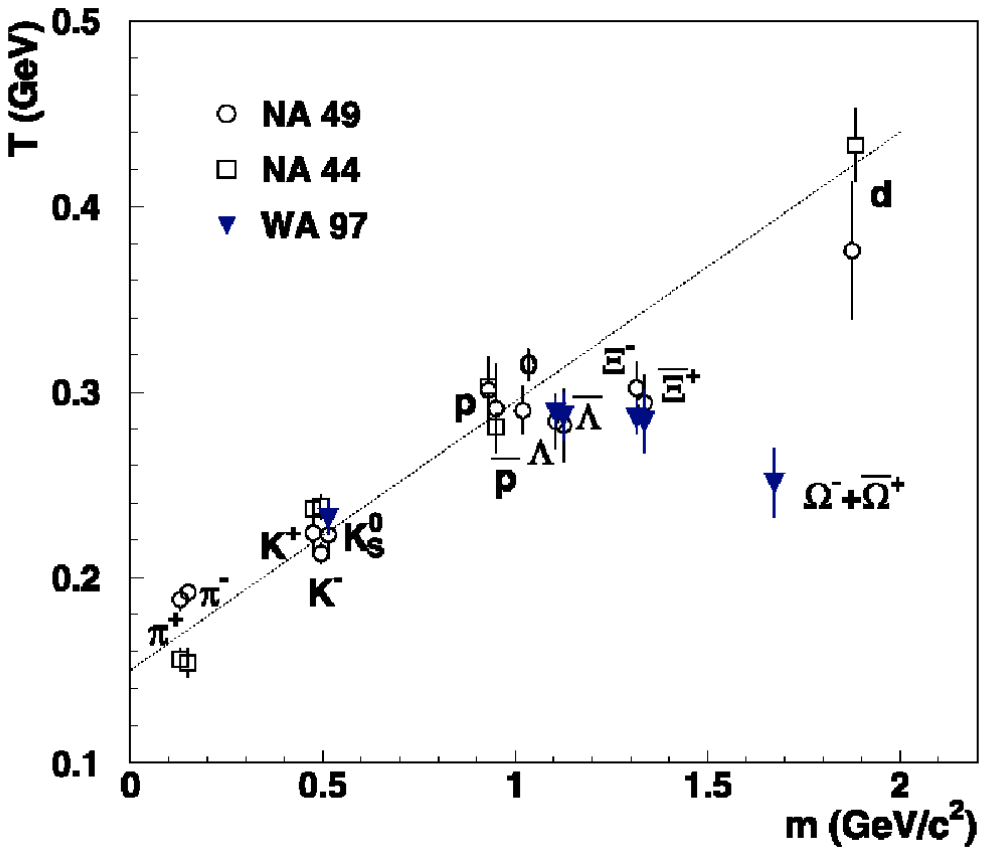

Figure 2.5: Dependencies of the m_T spectra inverse slopes T on the particle mass m for Pb+Pb collisions at the SPS energy.

Measurement of anti-particle and particle rations in heavy ion collisions can also give information on net baryon density. Figure 2.6 shows the anti-baryon to baryon ratio vs. $\sqrt{s_{NN}}$. The non-zero net baryon density is caused by stopping

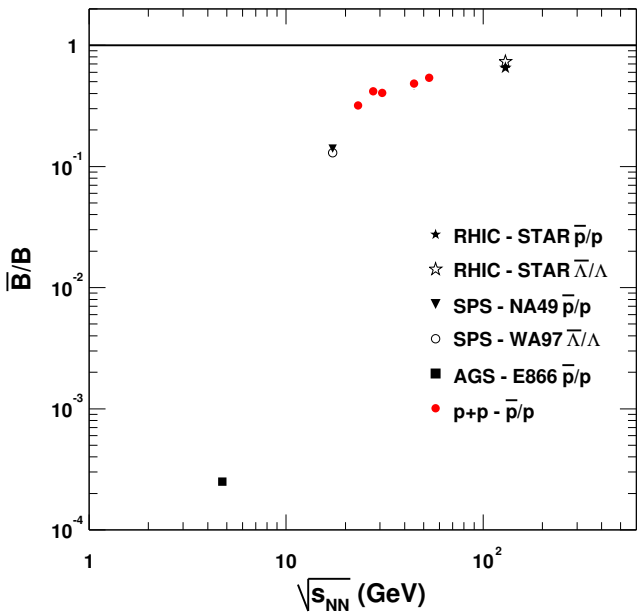

Figure 2.6: Anti-baryon to baryon ratio vs. $\sqrt{s_{NN}}$. Heavy ion data for $\bar{\Lambda}/\Lambda$ and $\bar{p}/p$ are shown as well as the $\bar{p}/p$ ratio from $p+p$ collisions. There is considerable stopping in heavy ion collisions at the AGS and SPS ($\sqrt{s_{NN}} = 4.9$ and 17.2 GeV, respectively). Year 2000 RHIC data at $\sqrt{s_{NN}} = 130$ GeV indicates that $B - \bar{B}$ pair production accounts for over half of the baryon number in the central rapidity region.

effects. It is directly related to how much energy is initially transfered from the projectiles to the system. It is obvious that from AGS to SPS to RHIC, we are approaching the baryon-free region at mid-rapidity. Low net baryon density doesn't neccesarily mean small energy transfer. It only means the energy transfer is small as compared to the initial energy. While the mid-rapidity region is almost baryon-free for the RHIC energy, there is still substantial net baryon density for the SPS energy. This means the initial condition is quite different for the collisions at SPS and RHIC. Therefore, it would not be a surprise to see different results from RHIC. In addition, the two different initial conditions will

add more constraints to some theoretical models. When finite baryon density is present, breaking the particle/antiparticle symmetry, the exact balance between s and $\bar{s}$ requires non-trival relations between the parameters characterizing the final state hadron abundances. These strangeness conservation constraints imply different particle distributions for different structures of the source [JT96]. In addition, results of strangeness production from WA97 and NA49 experiments at the CERN SPS indicated the strangeness has little dependence on centrality. Lighter ion data obtained previously also confirm the impression that strangeness production is basically constant throughout the SPS domain [Shu99]. From the baryon ratios, one can tell that the initial conditions are rather different from the SPS to RHIC. Therefore, it would be very interesting to compare the observations on strangeness production at the SPS to those at RHIC.

In strangeness production, the phase space occupancy, γ_s, is a very important parameter in the statistical model. γ_s=1 means the strangeness reaches chemical equilibrium. This can be derived from the numbers of Λ, $\bar{\Lambda}$, protons and anti-protons [JT96]:

$$\gamma_s^2 = \frac{\Lambda}{p}\frac{\bar{\Lambda}}{\bar{p}}. \tag{2.10}$$

There have been measurements of this ratio at both AGS and SPS. It was found the ratio is very high, considering the mass of the $\bar{\Lambda}$ is larger than the $\bar{p}$. Results from Experiment NA35 (Fig. 2.7) show the ratio in pp and pA reactions is small (< 1) and increase by almost a factor of 5 in S+S, S+Ag, S+Au reactions. A preliminary result for the ratio $\bar{\Lambda}/\bar{p}$ from NA49 is 3 ± 1 [Raf01b]. The AGS/E864 Collaboration has deduced a $(\bar{\Lambda} + \bar{\Sigma^0} + 1.1\bar{\Sigma^+})/\bar{p}$ ratio in Au+Au collisions at mid-rapidity and zero p_T. A strong increase of the $\bar{\Lambda}/\bar{p}$ ratio from peripheral to central collisions is deduced from experimental data at the AGS [Wan01](Figure 2.8). The large ratio in the mid-rapidity and low p_T region is mainly due

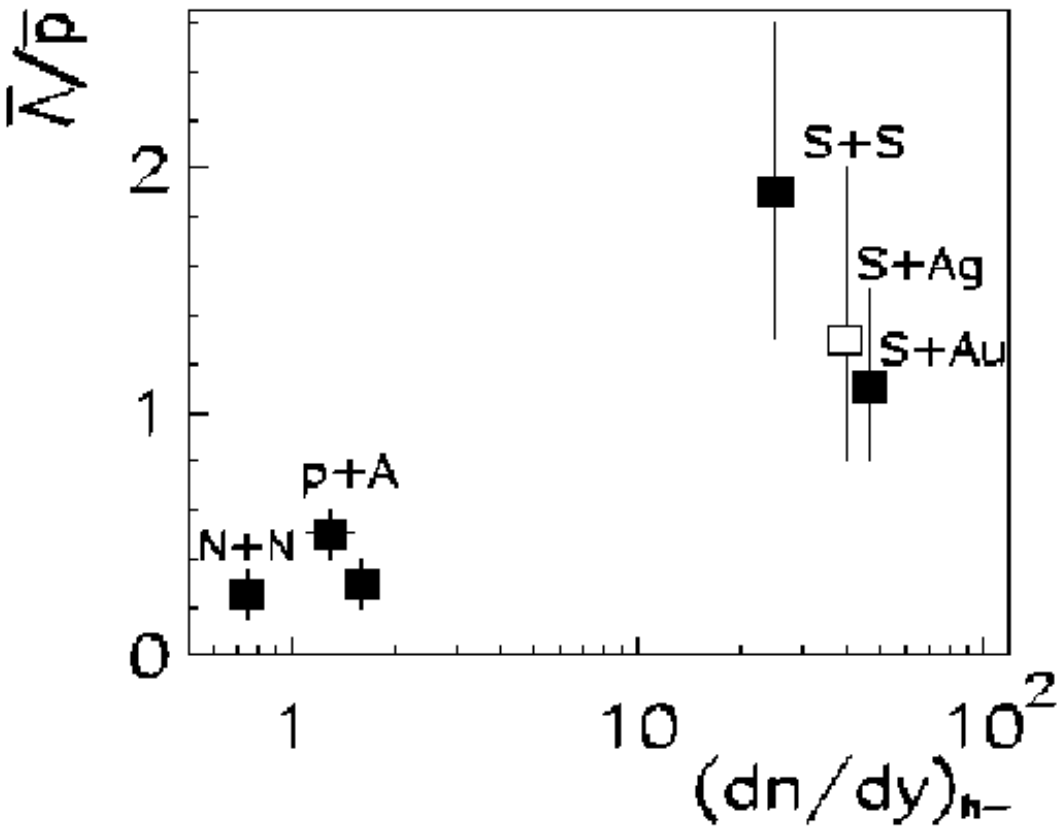

Figure 2.7: Ratio of $\bar{\Lambda}/\bar{p}$ at mid-rapidity as function of $dN/dy|_{h^-}$ from the CERN Experiment NA35.

to the strong absorption of the $\bar{p}$ and $\bar{\Lambda}$ [Wan01].

At RHIC, since the net baryon density at mid-rapidity is much smaller than that at the AGS or SPS, absorption effects should be much reduced. Therefore, the measurement of the ratio of $\bar{\Lambda}$ to $\bar{p}$ should be closer to the initial ratio.

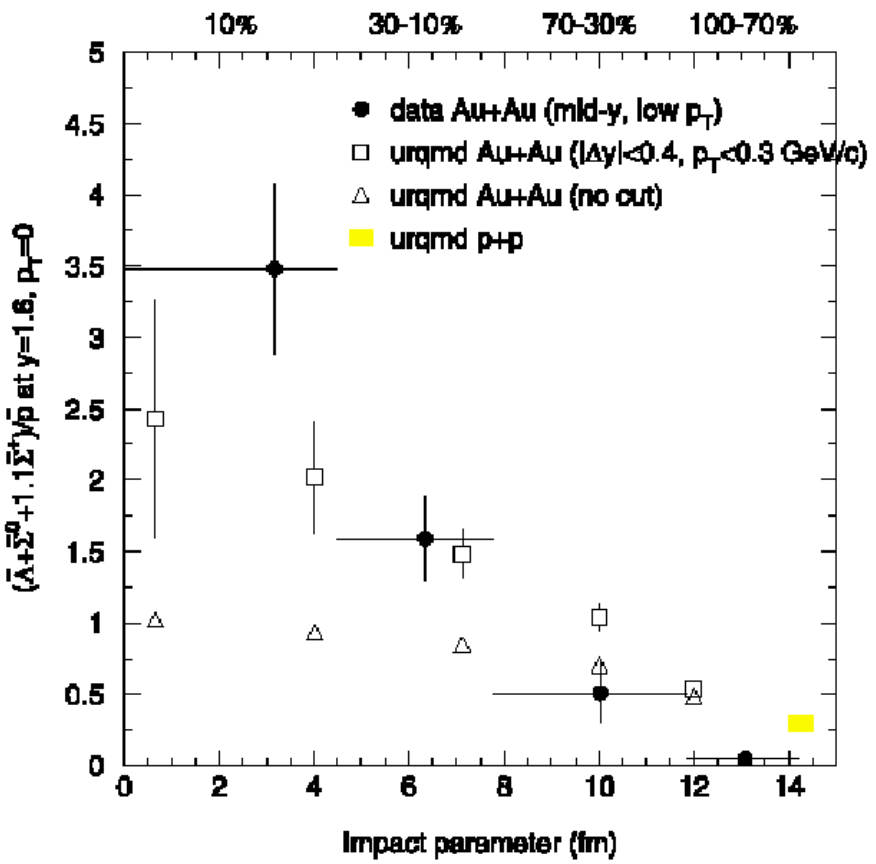

Figure 2.8: UrQMD calculation of the freeze-out $((\bar{\Lambda} + \bar{\Sigma^0} + 1.1\bar{\Sigma^+})/\bar{p}$ ratio at mid-rapidity $|\delta y| < 0.4$ and low P_T ($p_T < 300$ MeV/c)as function of impact parameter (open squares), compared with experimental results in a similar kinematic region (filled circles). Figure taken from [Wan01].

CHAPTER 3

Facilities

3.1 RHIC Accelerator Complex

The Relativistic Heavy Ion Collider is located at Brookhaven National Laboratory on Long Island, NY. The facility consists of two rings of superconducting magnets, each with a circumference of 2.4 miles. The whole RHIC complex (Figure 3.1) includes also the Tandem Van de Graaff accelerators, the Booster Synchrotron and the Alternating Gradient Synchrotron (AGS). Gold(Au) atoms are generated in the Pulsed Sputter Ion Source in the tandem. They are accelerated and passed through two Au foils to strip off some of the electrons from the atoms. That leaves a beam of Au atoms an energy of 1 MeV/nucleon and a distribution of charge states peaking at +32e. The 1 MeV/nucleon Au is then transferred to the booster where it is accelerated to 95 MeV/nucleon and further stripped to a net charge of +77e before it is injected to the AGS. In the AGS, the energy of the Au beam is increased to 10.8 GeV/nucleon and the beam is bunched. In the final stage of the injection into the RHIC rings, all the orbital electrons of the Au atoms are stripped off and the atoms have a charge of +79e. Once injected into RHIC, the bunches are accelerated to collision energy and kept in the rings by the magnetic fields produced by the superconducting magnets. For proton beams, the Linear Accelerator is used as the source instead of the tandem.

RHIC is the first machine in the world capable of colliding heavy ions. It can

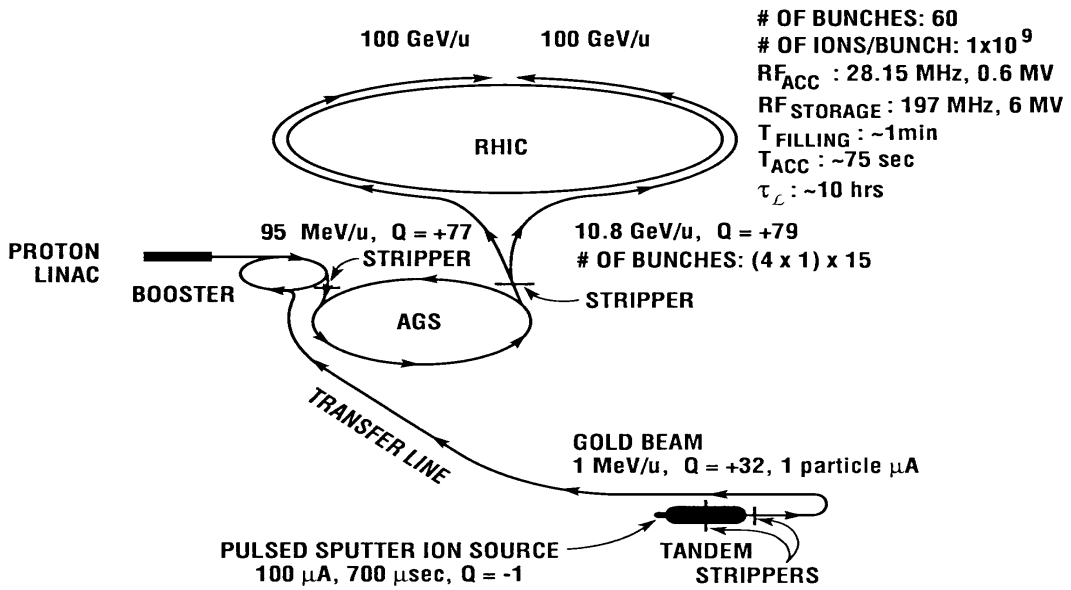

Figure 3.1: Diagram of the AGS - RHIC facility. .

Physical Parameters		
No. Intersection Regions	6	
No. Bunches/ring	60	
Bunch Spacing (nsec)	213	
Collision Angle	0	
Free Space at Crossing Point (m)	± 9	
Performance Specifications	Au	p
No. Particles/Bunch	1×10^9	1×10^{11}
Top Energy (GeV/u)	100	250
Luminosity, average ($\mathrm{cm}^{-2}\mathrm{sec}^{-1}$)	$\sim 2 \times 10^{26}$	$\sim 1 \times 10^{31}$

Table 3.1: Physical parameters and performance specifications for the Relativistic Heavy Ion Collider (RHIC).

be used to accelerate and collide species ranging from p+p @$\sqrt{s_{NN}}$=40-500 GeV to Au+Au @ $\sqrt{s_{NN}}$ = 40-200 GeV. This great flexibility allows physicists to study a variety of colliding systems at different energy levels. Table 3.1 lists the performance specifications for RHIC.

The RHIC ring has 6 intersection points where its two rings of magnets cross, allowing the particle beams to collide. Four of the interaction regions are currently occupied by 4 experiments, BRAHMS, PHOBOS, PHENIX and STAR. The first commission run occured in the summer of year 2000. At 9 PM on 12 June 2000, the first beam-beam collision event at RHIC at a collision energy of $\sqrt{s_{NN}}$ = 60 GeV was recorded by STAR (Figure 3.2). In Figure 3.2, the lines coming out from the center are the tracks left in the detector by the high velocity charged particles produced in collisions. A few weeks later, STAR recorded collisions at $\sqrt{s_{NN}}$ = 130 GeV, which is the nominal beam energy for the summer run in 2000 (Figure 3.3).

3.2 The STAR Detector

The physics program of the STAR experiment is to study not only soft physics processes, i.e. hadron production at transverse momenta below 1-2 GeV/c but also hard QCD processes, i.e. jet, mini-jet and hard photon production [Col92]. It aims to analyze momentum and identify charged particles (π^+, π^-, K^+, K^-, p, $\bar{p}$, d, $\bar{d}$) directly, as well as various neutral and charged particles (K^0_s, ϕ, Λ, $\bar{\Lambda}$, Ξ^-, Ω^-) via charged particle decay modes [Col92]. Its ability to study observables on an event-by-event basis makes it a unique detector at RHIC.

STAR (Figure 3.4) is a cylindrical detector system with 2π azimuthal coverage over the central rapidity region. The full configuration of the STAR detector in-

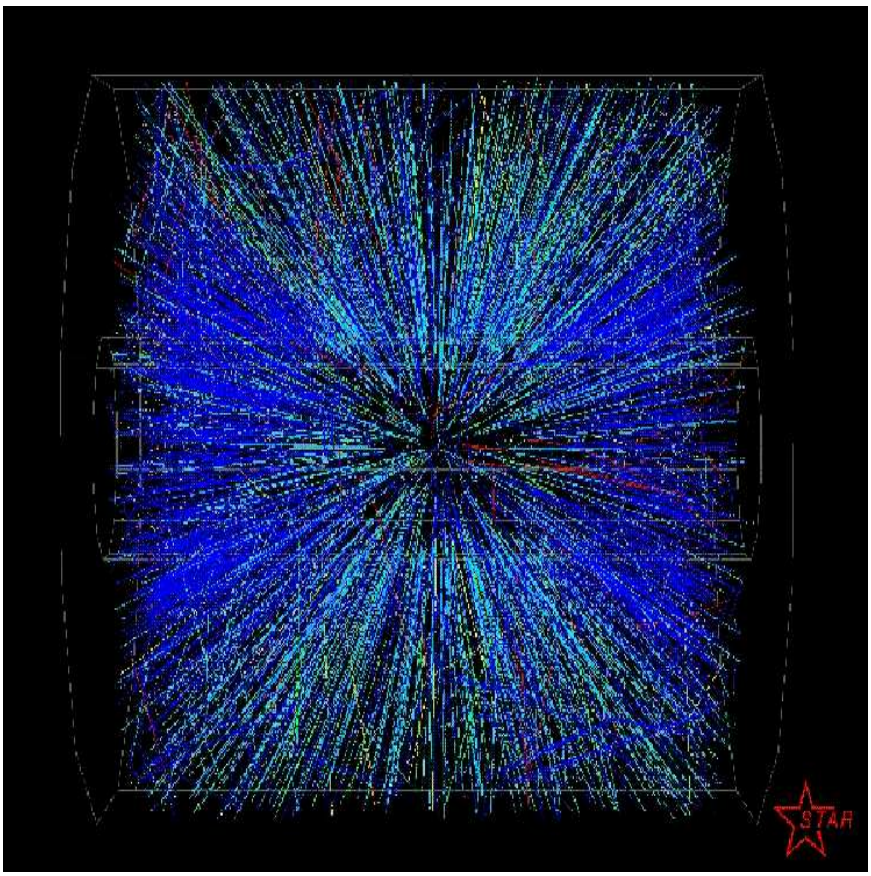

Figure 3.2: First collision at $\sqrt{s_{NN}} = 60$ GeV. Side view of TPC fiducial volume. Tracks are reconstructed from online level-3 trigger.

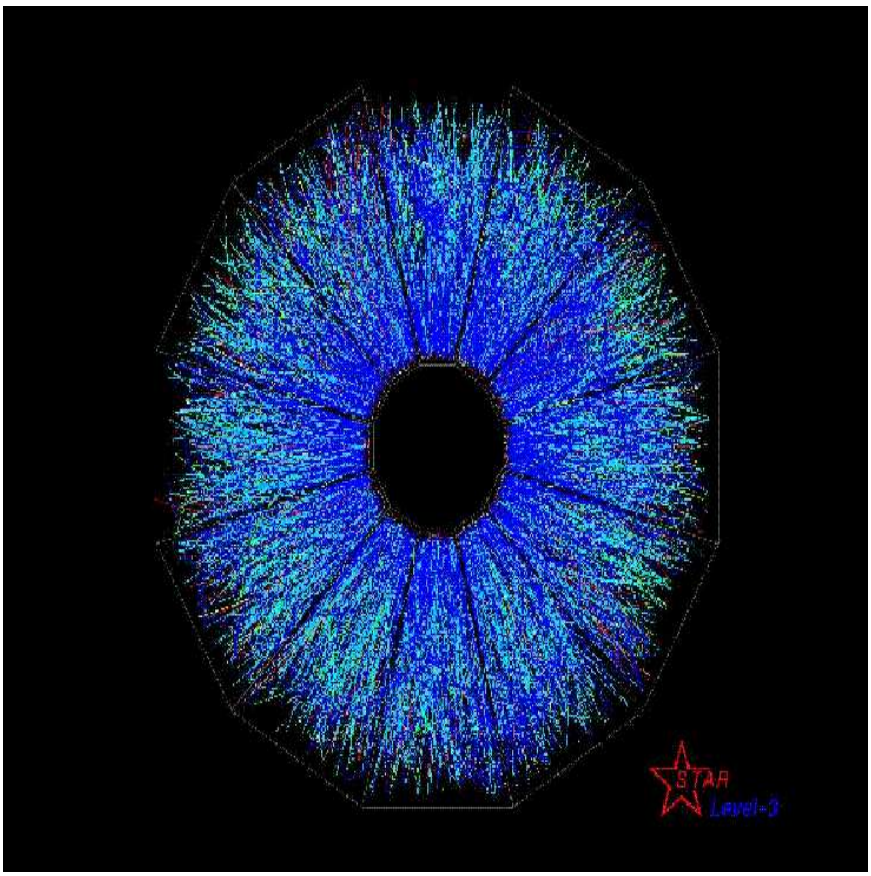

Figure 3.3: First collision at $\sqrt{s_{NN}} = 130$ GeV. End view of TPC fiducial volume. Tracks are reconstructed from online level-3 trigger.

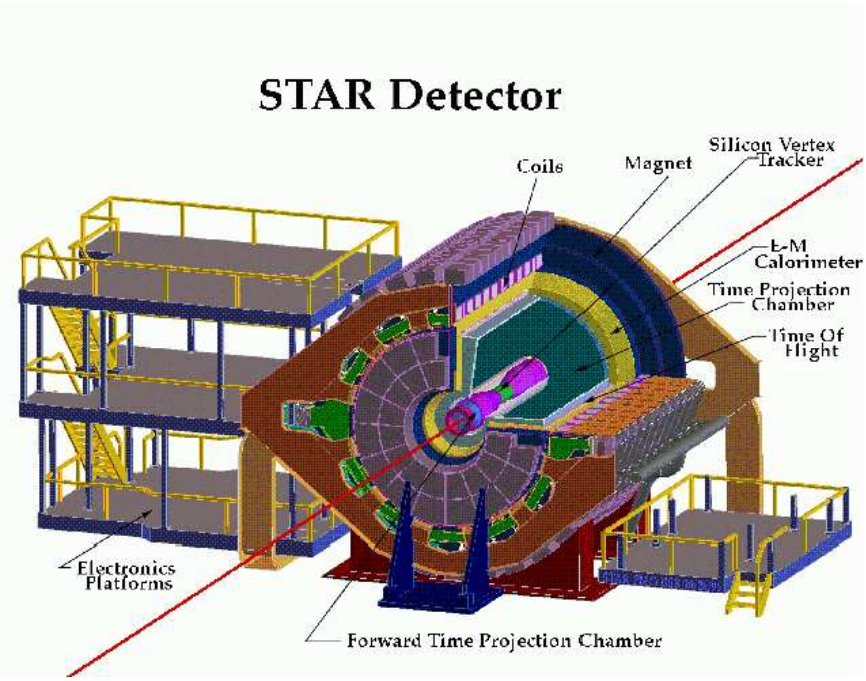

Figure 3.4: The STAR experiment.

cludes these sub-systems: Time Projection Chamber (TPC) [Ack99], Silicon Vertex Tracker (SVT), E-M Calorimeter (EMC), Forward Time Projection Chamber (FTPC), Central Trigger Barrel (CTB), Zero Degree Calorimeters (ZDC), Time of Flight (TOF) and magnet. For the year 2000 data-taking, the setup consisted of only the TPC, CTB, ZDC and one ladder of SVT. A ring-imaging Cerenkov detector (RICH) with an area of approximately one square meter is positioned directly outside the TPC for high-p_t particle id during the first two years of running.

The STAR magnet can provide uniform fields along the beam direction with a strength of 0.25 Tesla to 0.5 Tesla. For the Year 2000 physics run, the field was set at 0.25 Tesla. Figure 3.5 shows the mapped field [Tre00] in the radial direction at full field. The deviation from a uniform field is within the design value of 0.5% over the volume of the TPC. The mapped field was used in the

offline reconstruction to correct the position of hits on tracks. Figure 3.6 shows the ExB distortion in both radial and axial directions in the TPC due to the non-uniform B field.

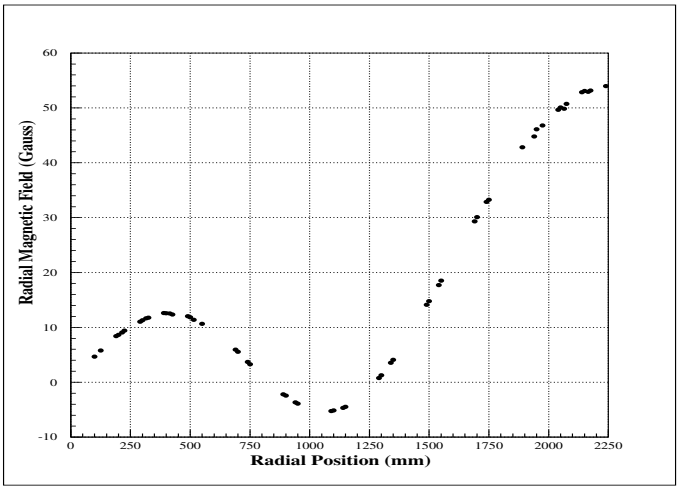

Figure 3.5: Radial component of the magnetic field as a function of radius at Z=210 cm. This plot demonstrates the uniformity of the magnetic at full field since the maximal deviation of the field within any volume will occur on the surface of that volume. The deviation is largest at the outer-most portion of the TPC starting from the center and changes sign from inner sector to outer sector ($r > 120$ cm). The mapped field was used in the offline correction.

The TPC is the main tracking detector of the STAR. It covers the pseudo-rapidity region -2 $< \eta <$ 2. Figure 3.7 is a perspective view of the STAR TPC. The TPC is divided into two longitudinal drift regions , each 2.1 m long, by a high voltage membrane. The inner field cage (r=0.5 m), the outer field cage (r=2.0 m) and the anode and pad sectors, which are 2.1 m away from the central membrane, define two coaxial cylindrical drift volumes of 24.75 m^3.

The chamber is filled with a gas mixture of 90% Argon and 10% Methane. The choice of the P10 gas for the TPC was made as a compromise among the

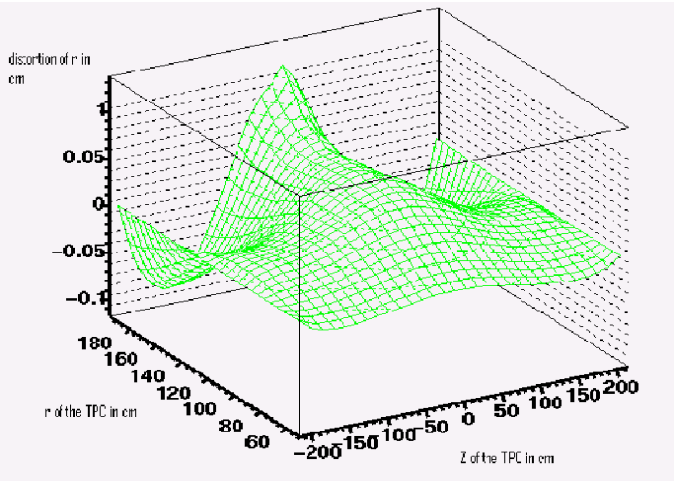

Figure 3.6: 3D view of ExB distortions. The calculated distortion on hit position caused by the ExB effects. The distortion is given as a function of R and Z for a single plane. The full map is computed as a function of 3D position in the TPC.

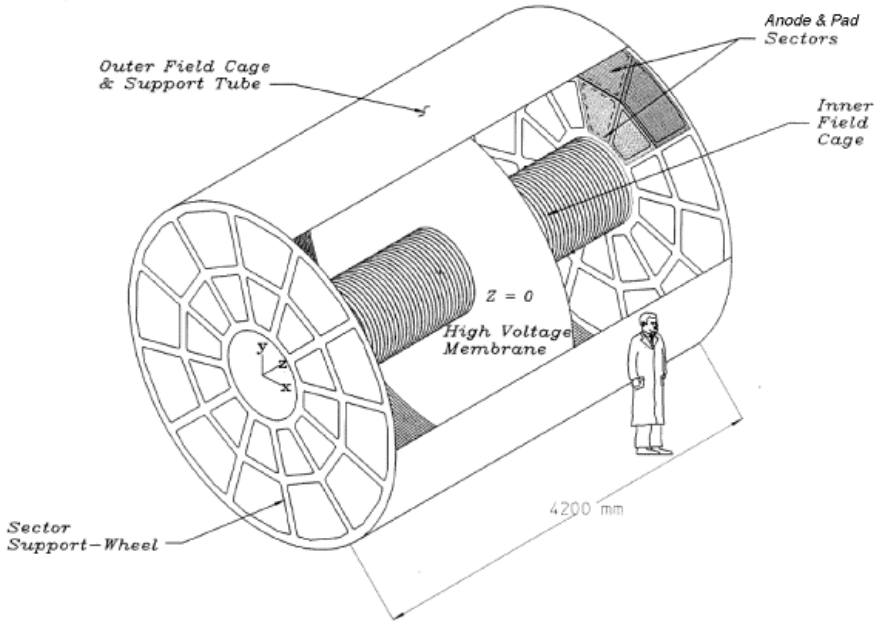

Figure 3.7: The STAR Time Projection Chamber.

following 10 features [Col92]:

1. The gas mixture has to work at atmospheric pressure ;
2. The electron drift velocity must be 2.0 cm/μs at $E < 300$ V/cm ; The field limit is determined by the tolerances of the insulators on the field cages;
3. At nominal field, the drift velocity should be saturated to reduce the effects from inhomogeneities in the E field, and variations from gas pressure (gas pressure changes with atmospheric pressure);
4. Small transverse and longitudinal diffusion;
5. Large $\omega\tau$, to reduce transverse diffusion;
6. High ionization efficiency;
7. Low electron absorption over drift length;
8. High drift velocity for positive ions in order to minimize the space charge accumulation;
9. Low rate of aging and high resistance to high voltage breakdown;
10. Gas should be cheap, safe and affordable in large quantities.

When a high velocity charged particle travels through the gas-filled TPC volume, the gas molecules will be ionized and produce positive ions and electron clouds along the path. The energy loss due to ionization is typically a few KeV per cm of gas. This gives a total energy loss of a few MeV over a path length of 2 m. For most particles produced in heavy ion collisions, the kinetic energy is above 100 MeV. Under the influence of the electric field provided by the central membrane (CM), inner field cage (IFC), outer field cage (OFC) and the grounded

anode plane, the electrons drift to the anode plane. The arrival time and locations of the electron clusters are recorded. Before the signals produced at anode plane can be read out by the electronics system, they are collected by the pads shown in the figure 3.8. The signals on pads are image charges induced by the electron avalanches in the region close to the anode wires where the E field is very strong.

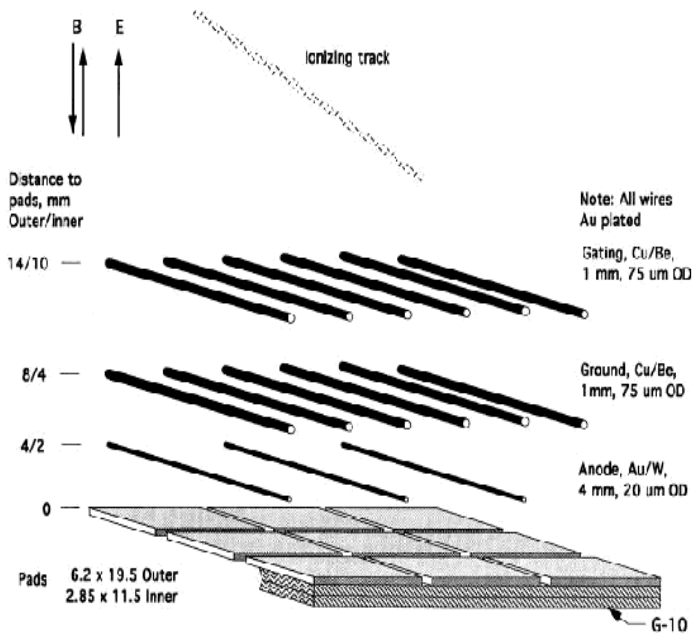

Figure 3.8: The Wires and Pads Layout. There are three layers of wires: gating grid, ground and anode wires. Each layer is equally spaced. The pad plane lies beneath the anode wires.

There are 144,000 pads grouped into 24 sectors, 12 on either end of the TPC and each with two subsectors (Figure 3.9), an inner subsector and outer subsector. The inner sector is made of 13 pad rows and the outer sector has 32 rows. A
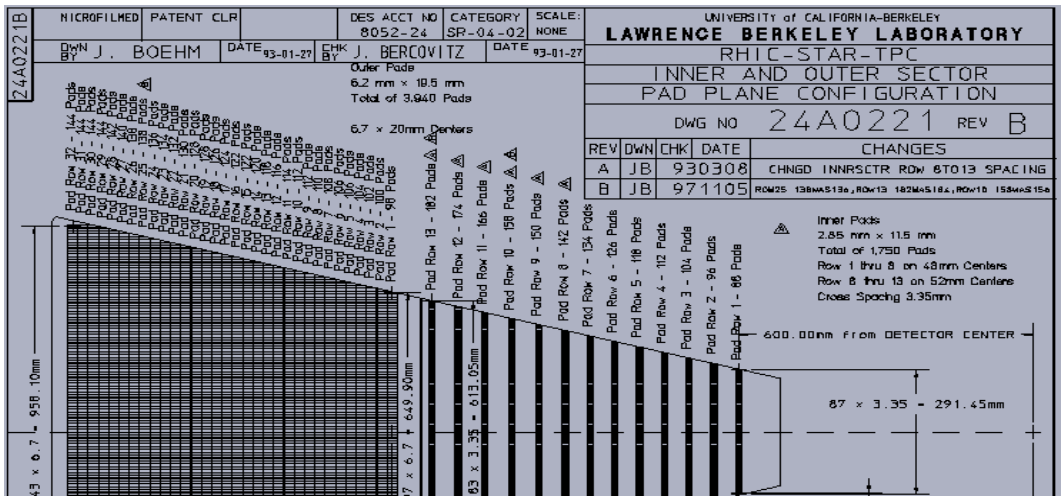
straight track passing through both sectors gives 45 dE/dx samples. This leads to a good ability in particle identification by means of energy loss measurements. The configurations of inner sector pads and outer sector pads are different. The sizes of pads were designed according to the required position resolution along pad row direction. With dimensions of 2.85 mm $\times$ 11.5 mm, the inner pads are smaller than the outer pads with dimensions of 6.2 mm $\times$ 19.5 mm. This gives them better two-track resolution, which is needed in the region where the track density is high.